JOURNAL OF GEOPHYSICAL RESEARCH, VOL. 101, NO. B10, PAGES 22,273–22,289, OCTOBER 10, 1996

Global lateral variations of shear wave attenuation in the upper mantle

Joydeep Bhattacharyya,[1] Guy Masters, and Peter Shearer
Scripps Institution of Occanography, Universily of California, San Diego

Abstract. We analyze several thousand high-quality, globally recorded $SS - S$ differential waveforms to constrain the lateral variation of shear wave attenuation (Q_β) in the upper mantle. We use a multitaper frequency domain technique to measure attenuation, parameterized by a t^* operator, and implement a robust estimation technique to compute t^* and its variance. The differential waveform technique minimizes the effect of factors such as finite source duration and structural complexity near the source and receiver so the differential $SS - S$ waveforms are mainly sensitive to the shear attenuation in the upper mantle under the SS bounce point. We use seismograms recorded at ranges of 45° to 100° and compute the $SS - S$ differential t^* from the broadening of the SS waveform relative to the Hilbert transform of the S waveform. A careful choice of fitting windows allows us to reduce the biasing effects of interfering phases which can affect t^* by up to 0.5 s. The t^* residuals (with respect to preliminary reference Earth model (PREM)) vary by ± 1.5 s with an average of ≈ 0.24 s. Our study suggests an average Q_β value of 112 (most of the lateral variations of Q_β are within 30% of this value) in the top 400 km of the mantle, slightly lower than the PREM value of 128. There is a qualitative correlation of t^* residual with tectonic region with distinctly higher attenuation observed under young oceans compared to platforms and shields. Also, the lateral variations of the residuals are similar in trend to those observed in studies of the attenuation of ScS multiples. At long wavelengths, the Q_β map shows a modest correlation with shear wave attenuation maps computed from surface wave analyses and with the patterns of lateral variations of shear velocities at certain upper-mantle depths predicted by the model $S16B30$. The correlation with the velocity model is highest at 300–500 km depth indicating that there may be a contribution to long-wavelength attenuation from relatively deep regions. Formal inversion for an upper mantle Q_β model shows that while lateral resolution is quite good, depth resolution is poor as might be expected. Better depth resolution must await combined body wave and surface wave inversions.

Introduction

Knowledge of the anelastic properties of Earth is important for many reasons. Since the attenuation of shear waves in Earth is primarily due to thermal relaxation processes [*Anderson and Minster,* 1980; *Minster and Anderson,* 1981; *Karato and Spetzler,* 1990], attenuation is a very sensitive indicator of temperature. In fact, laboratory experiments indicate that attenuation is a more sensitive measure of homologous temperature (the ratio of the temperature to the melting temperature) than are seismic velocities [e.g., *Sato et al.,* 1989], so attenuation can, in principle, be used to map regions in Earth which are close to the solidus. Furthermore, anelasticity causes physical dispersion [*Lomnitz,* 1957; *Lamb,* 1962; *Futterman,* 1962; *Jeffreys,* 1965; *Randall,* 1976; *Liu et al.,* 1976; *Kanamori and Anderson,* 1977], which means that the elastic moduli in Earth are frequency dependent. Because of this, *Karato* [1993] has shown that anelasticity can significantly affect the apparent relative temperature derivatives of seismic velocities and three-dimensional (3-D) variations in attenuation would inevitably lead to 3-D variations in these derivatives. This could have a significant impact on the construction of seismic tomographic models. Physical dispersion becomes even more important when seismic data with different characteristic frequencies are used in the construction of Earth models, a point which has been known since the mid 1970s [*Liu et al.,* 1976; *Anderson and Given,* 1982].

[1]Now at CIRES, University of Colorado at Boulder.

Paper number 96JB01782.
0148-0227/96/96JB-01782$09.00

Ideally, seismologists would solve simultaneously for the elastic and anelastic properties of Earth to get an internally consistent model. This is currently impractical due to the difficulty of isolating attenuation effects in the seismograms. The changes in waveforms due to attenuation (e.g., waveform broadening) are small compared to those due to changes in elastic velocities (e.g., travel times). Moreover, the observables that constrain attenuation (the amplitude, phase, and spectral content of the waveforms) are, in many cases, also affected by factors such as source complexity, multipathing, interference from other phases, and scattering and focusing due to heterogeneities. Thus Q measurements tend to be more scattered than travel time measurements and, in some cases, can differ considerably between studies.

One-dimensional (1–D) (radial) models of shear wave attenuation, Q_β, that are primarily based on free oscillation and/or surface wave data all agree that the upper mantle is the region of highest attenuation in the mantle [e.g., *Anderson and Archambeau,* 1964; *Kovach and Anderson,* 1964; *Anderson et al.,* 1965; *Anderson and Hart,* 1978; *Anderson and Given,* 1982; *Dziewonski and Steim,* 1982; *Dziewonski and Anderson,* 1981; *Widmer et al.,* 1991; *Durek and Ekstrom,* 1996] which is also where we expect the largest lateral variations to occur. Observations of fundamental mode frequencies and apparent attenuation rates have been inverted for lateral variations of shear wave attenuation in the upper mantle [*Smith and Masters,* 1989; *Roult et al.,* 1990; *Suda et al.,* 1991], but these studies are restricted to structure of even harmonic degree and have had limited success in explaining the observations. Several studies using surface waves (periods > 150 s) have also mapped the lateral variations of Q_β. For example, *Romanowicz* [1990] constrained the degree 2 component of global Rayleigh wave attenuation using combinations of multiple surface wave orbits to mitigate the effects of focusing and defocusing, an approach also followed by *Durek et al.* [1993].

Recently, *Romanowicz* [1994a] presented a variation of this technique which allows information about odd-order attenuation structure to be retained and has applied this method to develop a large-scale (roughly equivalent to harmonic degree 6) 3-D model of mantle attenuation structure [*Romanowicz,* 1994b, 1995]. These studies reveal lateral variations of attenuation, with most of the attenuation limited to depths shallower than 400 km. Several regional studies using the the first Rayleigh wavetrain also show substantial variability of upper mantle shear attenuation at shorter length scales [*Mitchell,* 1975; *Mitchell et al.,* 1977; *Canas and Mitchell,* 1978, 1981; *Nakanishi,* 1979b; *Bussy et al.,* 1993]. These surface wave studies find a correlation between slower phase velocities and higher attenuation, suggesting a common thermal origin for both velocity and attenuation perturbations in the mantle.

At higher frequencies, body wave measurements have been used to study the attenuation of the mantle. Such measurements can be complicated by the effects of interfering waveforms, source and receiver structure, scattering, multipathing, and frequency-dependent attenuation where the corner of the mantle absorption band is close to body wave frequencies [*Sipkin and Jordan,* 1979; *Anderson and Given,* 1982; *Sipkin,* 1988]. Regional-scale attenuation studies typically have used long-period waveforms (dominant period $\approx$ 20 s) since effects such as scattering and multipathing are greatly reduced in this type of data and signal levels are high. Most such studies have concentrated on multiple ScS phases to give a measure of the whole mantle averaged Q_β under a particular region. *Nakanishi* [1979a], *Sipkin and Jordan* [1980], *Lay and Wallace* [1983, 1988], *Chan and Der* [1988], *Revenaugh and Jordan* [1989, 1991], and *Sipkin and Revenaugh* [1994] present estimates of Q_{ScS} in many different parts of the world and find differences between regions that imply very large variations in mantle attenuation if the signal is confined to the upper mantle (see below). Other differential phases have been used to analyze regional Q_β structures. For example, *Schlue* [1981], *Sheehan and Solomon* [1992], and *Ding and Grand* [1993] have used multiple S phases, while *Flanagan and Wiens* [1990, 1994] have used depth phases together with the direct arrivals to constrain the attenuation structure in back arc regions of the upper mantle. These studies also suggest considerable lateral variation in shear wave attenuation.

In this study, we analyze differential $SS - S$ waveforms from long-period transverse component seismograms recorded at Global Seismic Network (GSN) stations. The differential broadening observed between the two waveforms is used to constrain the lateral variations of shear wave attenuation in the upper mantle. We use a much larger data set relative to earlier studies and have substantially better global coverage. The waveforms have dominant periods of $\approx$ 20 s and so have horizontal wavelengths of a few hundred kilometers and are expected to average much of the local heterogeneities along the ray path. Figure 1a shows the ray geometry of these two phases. We expect that the observed differential broadening is explained by attenuation in the upper mantle near the SS bounce point. We can see from Figure 1a that our data are relatively insensitive to structure beneath the source and receiver where the S and SS ray paths are nearly coincident. Figure 1b shows an example of a seismogram used in this study; the SS phase is Hilbert transformed with respect to the S phase [*Choy and Richards,* 1975]. Although the Hilbert transform is a high-frequency approximation, we will demonstrate in a later section that it is an excellent approximation for our data.

The next section describes a frequency domain measurement technique which can use information from both the amplitude and phase spectra of the two waveforms. Application of the technique to synthetic seismograms for a variety of test structures allows us to evaluate the many sources of bias encountered in such

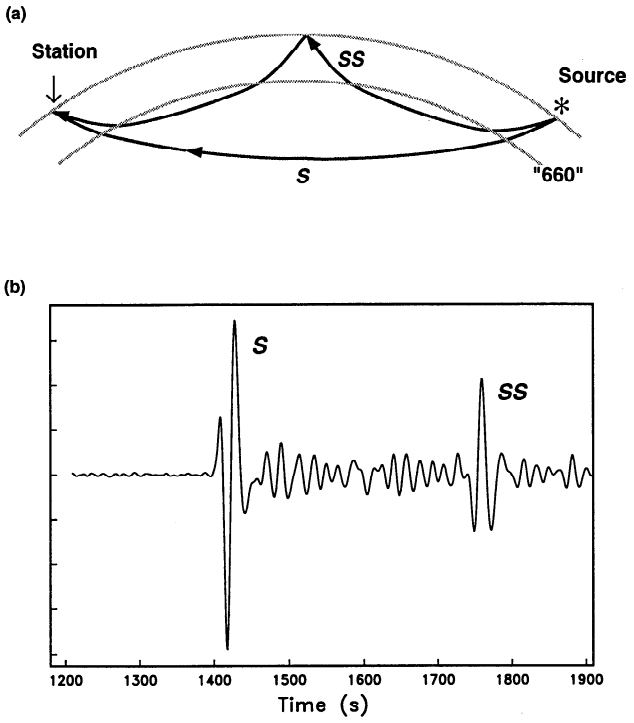

Figure 1. (a) Schematic diagram showing the ray geometry. (b) Long-period seismogram showing the S and the SS phases. The SS waveform is clearly Hilbert transformed with respect to the S waveform. Differential broadening between the waveforms is explained by attenuation near the SS bounce point.

studies. We conclude that the method gives robust estimates of attenuation and apparently gives more stable results than time domain methods. The technique also provides an estimate of the error in our measurements. These a priori error estimates are then used in a stacking technique to give yet more stable estimates of attenuation. A discussion is given of our observations and we conclude with a preliminary inversion for shear Q structure in the upper mantle.

Theory and Measurement Technique

Theory

In our differential waveform measurements, the S and the SS phases propagate through similar structure beneath the source and the receiver. We therefore expect that the relative attenuation between the two pulses is mainly accumulated near the SS bounce point. We use an absorption band operator to model this differential attenuation [e.g., *Liu et al.*, 1976; *Anderson et al.*, 1977; *Lundquist and Cormier*, 1980; *Bhattacharyya et al.*, 1993a] so that the transfer function $T(\omega)$ between the spectra of the Hilbert-transformed S wave and the SS wave can be written as

$$T(\omega) = Ae^{-\omega t^* c_1(\omega)} e^{-i\omega t^* c_2(\omega)} e^{-i\omega t_0} \tag{1}$$

where A accommodates the excitation differences between S and SS, t_0 is the time separation between the two pulses, and t^* is defined as

$$t^* = \int \frac{{Q_m}^{-1}}{c_\infty} dx \tag{2}$$

The integral is taken along the ray path, Q_m is the peak value of Q within the absorption band, and c_∞ is the seismic velocity at the infinite frequency limit. The expressions for $c_1(\omega)$ and $c_2(\omega)$ are determined by the specific properties of the absorption band operator. We use the operator described by *Doornbos* [1983]:

$$\begin{aligned} c_1(\omega) &= \frac{1}{\pi} \tan^{-1}\left[\frac{\omega(\tau_2 - \tau_1)}{1 + \omega^2 \tau_1 \tau_2}\right], \\ c_2(\omega) &= \frac{1}{2\pi} \ln\left[\frac{1 + 1/\omega^2\tau_1^2}{1 + 1/\omega^2\tau_2^2}\right] \end{aligned} \tag{3}$$

where τ_1 and τ_2 (assumed to be independent of depth) are the lower and upper relaxation time constants describing the edges of the absorption band. Since we are looking at relatively long-period body waves, it is reasonable to suppose that we are in the middle of the absorption band ($\omega\tau_1 \ll 1$ and $\omega\tau_2 \gg 1$) where $c_1 \approx 0.5$ and c_2 can be separated into two parts:

$$c_2 \simeq \frac{1}{\pi} \ln\left[\frac{1}{\tau_1}\right] - \frac{1}{\pi} \ln[\omega] \tag{4}$$

The first term results in a time shift of the whole waveform which is sensitive to the poorly known lower cutoff of the absorption band; so we incorporate this term into t_0. The second term gives a frequency-dependent phase shift which is proportional to t^*, so we can, in principle, use the phase of the transfer function, as well as the amplitude, to constrain attenuation. Given these approximations, the transfer function is insensitive to the exact values of τ_1 and τ_2 and so is parameterized solely by the value of t^*.

Measurement Technique

The frequency domain analysis adopted in this study is based on the multitaper technique of spectral estimation of *Thomson* [1982]. A series of tests [*Bhattacharyya et al.*, 1993b] (and below) have shown that this technique gives less biased estimates of attenuation when compared with a time domain technique involving cross correlation of waveforms. Suppose $X_i(\omega)$ is the spectrum of the Hilbert-transformed S pulse multiplied by the ith taper and $Y_i(\omega)$ is the corresponding spectrum of the ith-tapered SS pulse, then

$$Y_i = TX_i \tag{5}$$

where T is given by equation (1).

For the record lengths of the windowed S and SS phases typically available to us (35–50 s), we can use three 2π-prolate tapers and still obtain sufficient fre-

quency resolution to estimate attenuation. We compute the t^* value for each record using two different methods: (1) fitting slopes to the amplitude of the ratio of the spectral estimates of the SS and S waveforms, and (2) solving for the transfer function between the two waveforms. Using both these methods gives an internal consistency check on the measurements. For the amplitude spectrum, at each frequency we have

$$\ln\left[\frac{|\mathbf{X}^* \cdot \mathbf{Y}|}{\mathbf{X}^* \cdot \mathbf{X}}\right] = \ln(A) - \omega t^* c_1 \qquad (6)$$

and an equivalent expression for the phase (the individual taper estimates in $\mathbf{X}$ and $\mathbf{Y}$ may be weighted differently in the dot products; see *Thomson* [1982] for details). We usually have three independent spectral estimates across the frequency band where we have signal (0.02–0.1 Hz); thus six data (amplitude and phase at three frequencies) constrain three unknowns (A, t_0, and t^*). If we use only amplitude information, we have three data and two unknowns. We solve the system using the QR algorithm given by *Lawson and Hanson* [1974].

Since we have more data than unknowns, we can get a rough estimate of the precision of our measurement. At each frequency point we use different combinations of the three orthogonal tapers to compute the delete-one jack-knife [*Efron*, 1982] variance of the estimate at that frequency. This gives us an estimate of the variance of the spectral ratio at each frequency point. We compute t^* from the best fitting slope to these spectral ratios (weighted by their errors). We then use a bootstrap method [*Efron*, 1982] to compute an estimate of the error in the slope. For each frequency, we randomly select a value which is normally distributed with the spectral ratio as mean and the variance equal to the jack-knife estimate. We repeat this process for all of the frequency points and then calculate the slope. We carry out this slope fitting 200 times to obtain 200 estimates of differential t^*. The standard deviation of this distribution gives us a measure of the variability of t^*, providing an error estimate for the measurement from each seismogram.

The differential waveform measurement technique is illustrated in detail in Figure 2. The following steps are made for each measurement:

1. The direct (S) and the reflected (SS) waveforms are windowed (as in Figure 2a). The S waveform is then convolved with a t^* operator of 3.0 s which is roughly equal to the theoretical prediction of the mean differential t^* for $SS - S$ (according to the preliminary reference Earth model (PREM), the differential t^* varies between 2.8 and 3.1 s for the rays considered in this study).

2. After the S phase is Hilbert transformed, a least squares fitting procedure is used to best align and scale the two waveforms (see Figure 2b).

3. The window used for the spectral fitting is chosen in this step. Since proper window selection can reduce the primary source of bias (interference from nearby phases), a certain amount of flexibility is allowed in the selection of the actual waveforms for t^* calculation. We experiment with a number of fitting windows and choose the longest window (with highest-frequency resolution) which gives a stable spectral estimate. Figure 2c shows the spectra of the SS (solid) and the processed S (dashed) phases. Seismograms which show rapid changes of spectral shape for either of the phases are discarded.

4. We estimate the differential t^* for the windowed waveforms using both frequency domain methods described above. Figure 2d shows the fit to the t^* model using the method of fitting to the (logarithmic) amplitude spectrum.

5. Based on our confidence in the measurement, we assign a grade of A, B, or C to the residual t^* value. These grades reflect the level of interference from nearby waveforms and our confidence in the spectral fits. We use the average error of the measurements for each quality as a representative error for a measurement of that quality.

Assessment of Bias in Individual Measurements

There are many factors which can bias attenuation measurements, and this section presents some experiments with synthetic seismograms which attempt to identify the main problems. The synthetics are made using a toroidal-mode summation technique for a variety of simplified Earth models where each model is designed to isolate a particular source of bias. In each experiment, we attempt to recover the best fitting t^* operator which maps the Hilbert-transformed S waveform to the SS waveform. These best fit t^* values are compared with theoretically predicted values for that model (computed using ray tracing through the model). The tests are summarized as follows.

Testing the t^* model and the validity of the Hilbert transform approximation. This experiment uses a simple Earth model with velocity and density profiles which are quadratic polynomials in radius, depth- and frequency-independent attenuation (Q_β), and a logarithmic physical dispersion law (with a reference period of 1.0 s). The model does not have a core, mantle discontinuities, or a crust. We find that the the absorption band (i.e., t^*) model gives excellent fits to the waveforms (Figure 3a) and the inferred value of t^* matches that produced by ray tracing using equation (2) (Figure 3b). Thus the t^* model is quite capable of modeling the differential attenuation in long-period seismograms.

We have also made synthetic seismograms for this model with no attenuation so that we can test the Hilbert transform approximation. We find that the best fitting phase shift is 90° (i.e., the Hilbert transform approximation holds) until an epicentral distance of about 120° and the Hilbert-transformed S is visually indistinguishable from SS (Figure 3c). We thus conclude that the Hilbert transform is an excellent approximation for

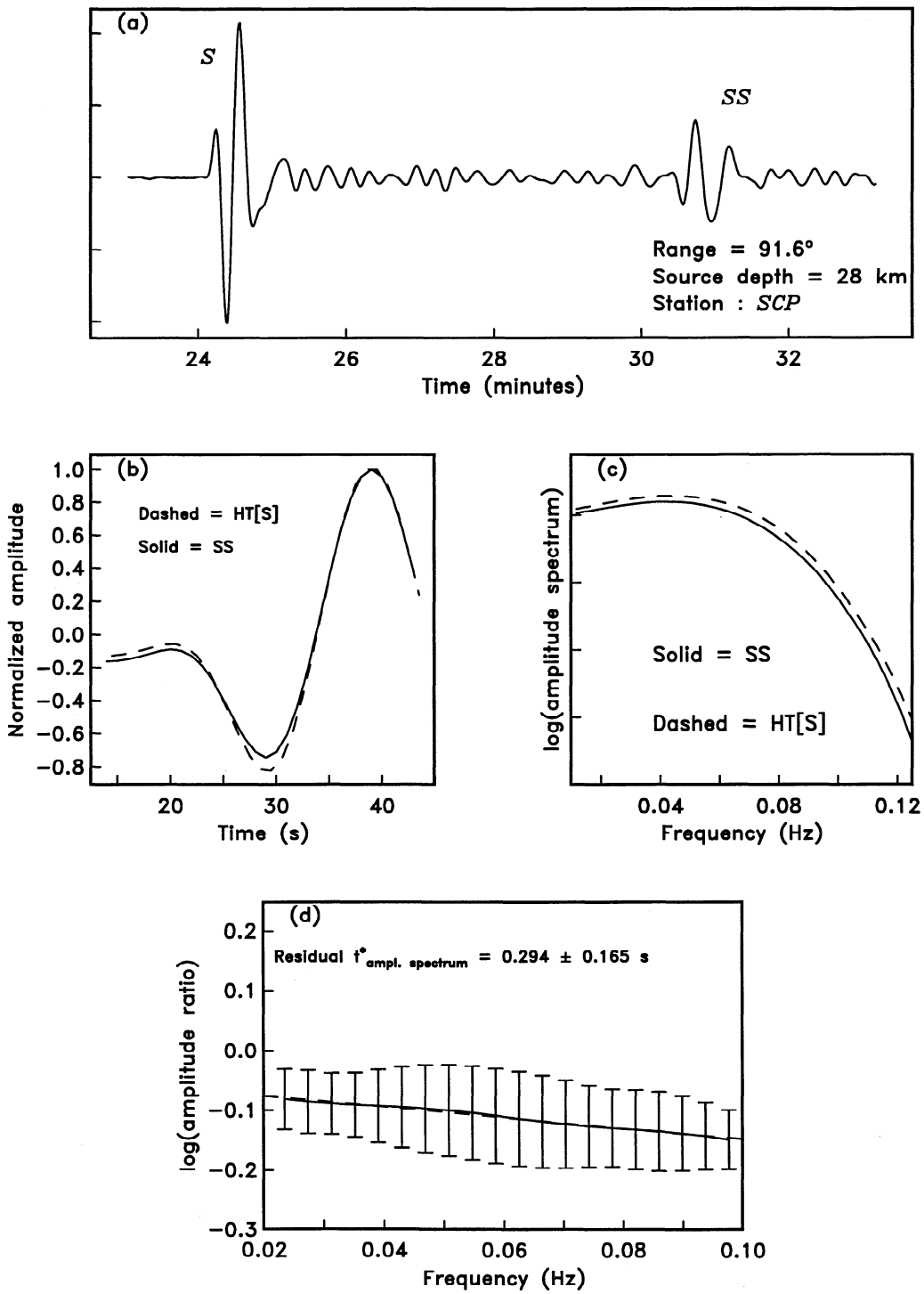

Figure 2. An illustration of the differential t^* measurement technique used in this study. (a) Seismogram showing the S and the SS waveforms. (b) Aligned and scaled (using a least squares method) S and SS phases. (c) Spectra of the Hilbert-transformed S (dashed) and the SS (solid) waveforms computed using the multiple taper spectral estimation technique. (d) The value of t^* measured from the best fitting slope to the amplitude of the ratio of the two spectra.

the long-period seismograms in the distance range of our study (45°–102°).

Crustal reverberations under the SS bounce point. The effect of the crust is investigated with two models differing in their crustal thicknesses (35 km and 20 km) and with a representative Moho impedance contrast (0.17) as given by the Parametric Earth Model, Continental (PEMC) [*Dziewonski et al.*, 1975]. The precursor due to the bottomside reflection and the postcursor due to the topside reflection at the Moho under the SS bounce point can both interfere with the SS phase. For 35-km-thick crust, we obtain measurement errors of up to 0.25 s but with no systematic bias. For 20-km-thick crust, an error of up to 0.4 s can occur and tends

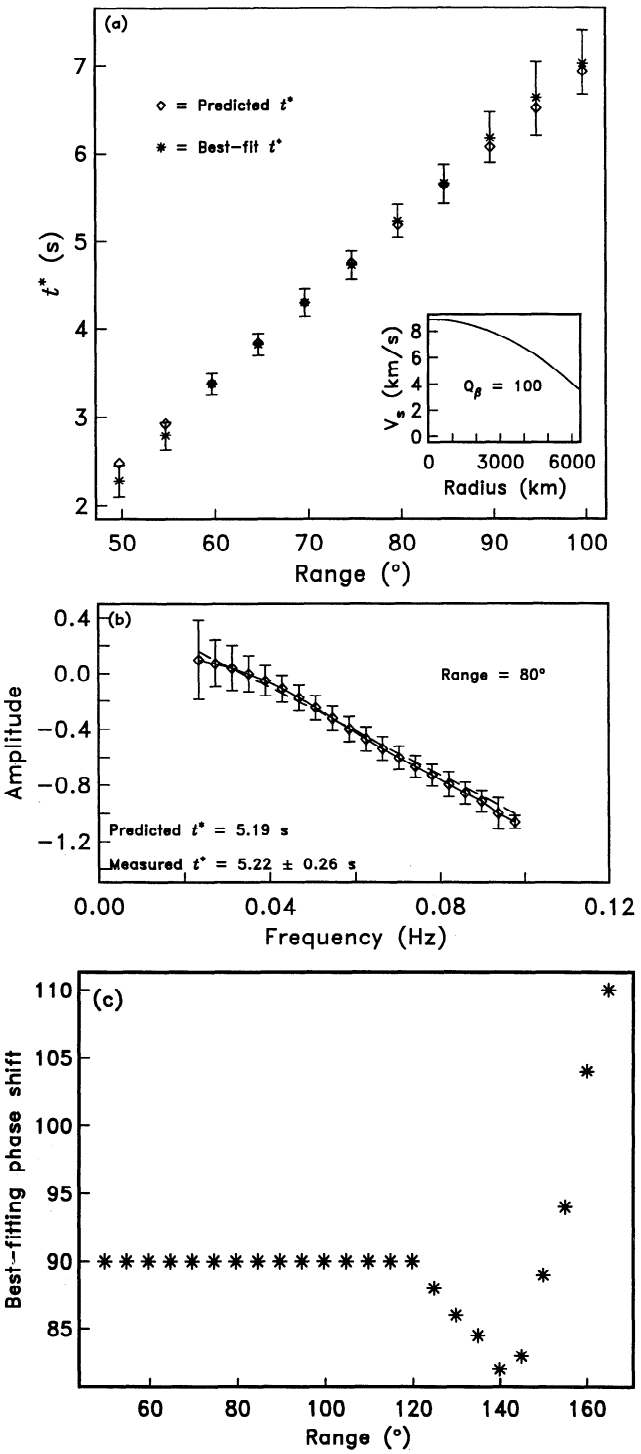

Figure 3. Results from testing the validity of the t^* model and the Hilbert transform approximation. (a) Comparison between the predicted t^* and values measured for synthetics computed for a model with a quadratic velocity profile and constant shear attenuation (inset) at different epicentral distances. (b) An example of the fit for a synthetic seismogram computed for the above model at a distance of 80°. The measured value is very close to the value predicted by ray tracing. (c) The phase shift required to best fit the S waveform to the SS waveform for synthetics computed using a nonattenuating Earth model with the velocity profile shown in Figure 3a. This demonstrates that up to 120° distance, the best fitting phase shift is 90° (i.e., the Hilbert transform holds for long-period waveforms).

to be biased toward negative values (about -0.2 s for most distance ranges).

Upper mantle discontinuity phases. The topside or underside reflections from upper mantle discontinuities (particularly the 410-km and 660-km discontinuities) can give rise to significant phases in the data [*Shearer*, 1991]. At distances of less than about 65°, the precursor to SS due to an underside reflection from the 660-km discontinuity can significantly interfere with S, and the postcursor to S due to a top-side pegleg multiple from the 660-km discontinuity can interfere with SS. Moreover, the 660-km precursor to SSS can interfere with SS at all distances less than about 85°. We experimented with two Earth models, neither of them having a crust: one with only the 400 and 670, and one with all the upper mantle discontinuities as in PEMC. The results from both these models are very similar and lead to a scatter in the estimated t^* values of as much as 0.5 s at distances less than 85° with a negligible effect at greater distances.

The effect of ScS. To investigate this factor, we use a realistic Earth model except for the fact that it is smooth throughout the mantle (to remove the effects of mantle discontinuities). The effect of ScS on the S waveforms is greatest at ranges of about 90°–95°and can introduce errors of up to 0.4 s in the differential t^* measurements (though it is interesting to note that the real data show no increase in scatter in this distance range). At short distance ranges (less than 55°) the interference of ScS with the SS waveform leads to errors in differential t^* which are less than 0.2 s in magnitude and again are variable in sign.

Depth phases, sS and sSS. The depth phase is studied using nonattenuating, nondispersive, quadratic polynomial (i.e., no core, crust, or discontinuities) Earth models. We tried sources at 32, 64, and 128 km depths and, as might be expected, found the largest effects for the shallowest source. Even in this case, the effect was fairly random as a function of distance and rarely induced an error in t^* of greater than 0.1 s.

Effect of scattering and focusing/defocusing. Three-dimensional velocity variations will also have some influence on the waveforms. Amplitude variations due to focusing/defocusing effects should not bias our t^* values since we do not use the amplitudes in our analyses. However, to some extent, scattering and multipathing due to 3-D structure can cause pulse width distortion on individual seismograms. A full exploration of these effects will require experiments involving computation of synthetic seismograms at 15 to 25 s period for models with small-scale 3-D variations in elastic properties. Such an analysis is beyond the scope of this paper; also, it is unclear if current tomography models are accurate enough for the results to be meaningful. We expect that scattering effects will be relatively small at the long periods used in this study (very little coda is observed following the main arrivals). We also might expect that scattering/multipathing will result mainly from lateral velocity gradients and thus probably vary

on shorter spatial scale lengths than the Q variations. In this case our averaging scheme will reduce the bias from these effects.

We conclude from these experiments that the main cause of scatter in the observed t^* measurements is interference from other phases (particularly ScS and discontinuity phases). Careful choice of fitting window can reduce this bias, and use of the frequency domain measurement technique often allows contaminated arrivals to be identified (from the characteristic holes in their spectra) and discarded. These experiments suggest that we might expect a scatter in t^* of up to 0.5 s due to interference effects, yet the observed scatter from the individual measurements is greater than this. We believe that at least some of this additional scatter is due to lateral variations in attenuation in the mantle.

Application to Real Data

Analysis of Individual Records

We use only those long-period, transverse-component seismograms that have S and SS waveforms with high signal-to noise ratio and where we can clearly isolate both waveforms from interfering phases. We select events with $m_b \geq 5.5$ recorded at epicentral distances between 45° and 102° in the years 1976–1991. Seismograms recorded between 1976 and 1987 were those used in the study of $SS - S$ differential travel times by *Woodward and Masters* [1991]. We analyze only those waveforms which have a good S versus SS correlation; that is, those graded with A or B quality fits (see Woodward and Masters for a discussion of pick quality). For seismograms recorded after 1987, we select the highest-quality long-period data recorded at GSN (1988–1991) stations as obtained from the Incorporated Research Institutions for Seismology's Data Management Center (IRIS DMC). We discard contaminated seismograms where either the S or the SS waveforms interferes with other nearby waveforms or where the spectra are complicated. These criteria lead to a final data set of 3102 measurements. As noted by *Woodward and Masters* [1991] in their travel time study of $SS - S$, the clearest observations of S and SS waveforms occur at 80° to 102° range; hence these data constitute most of our measurements.

In the epicentral distance range of our study, both SS and S bottom at different depths in the lower mantle. As shown by *Woodward and Masters* [1991], the primary signal in $SS - S$ travel time residuals is accumulated in the upper mantle. This is probably more so in the case of residual t^* measurements since previous studies [*Widmer et al.*, 1991; *Revenaugh and Jordan*, 1991; *Durek et al.*, 1993; *Flanagan and Wiens*, 1994; *Romanowicz*, 1995] have shown that shear wave attenuation in the mantle is concentrated in the upper 300–400 km. Since the ray path of the SS phase is within 30° of vertical incidence for epicentral distance ranges above 50°, it is reasonable to assume that the differential measurement gives a localized sampling of the upper mantle beneath the SS bounce point.

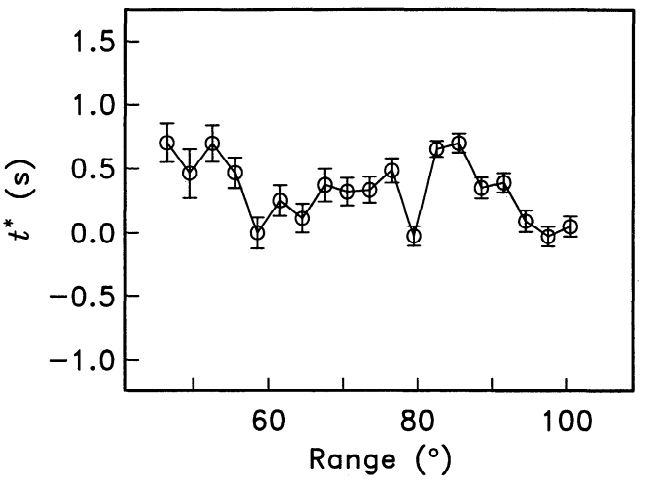

Figure 4. $SS - S$ residual t^* measurements (relative to PREM) plotted as a function of epicentral distance. The symbols show the medians of the residuals in 3° distance bins. A slight distance dependence is observed for ranges below 50° and above 95°.

Figure 4 shows the distance dependence of the residual t^* measurements (relative to the predictions of PREM) plotted as medians in 3° bins. We do not see any obvious trends in the data, and the average value remains quite constant ($\approx$ 0.4 s.) This suggests that the upper mantle Q_β structure is close to PREM (see below for details). The t^* values are found to be slightly higher for ranges below 50° and slightly lower for ranges above 95°, most probably due to the interference from the ScS phase at the front-end of SS and the back-end of S, respectively. Figure 5 shows the histograms for the different quality measurements. The median values of the seismograms are nearly same, though the spread (as given by the scaled median absolute difference, SMAD [*Kleiner and Graedel*, 1980]) of the residuals increases for lower quality measurements, as might be expected (0.18 s for the A picks, 0.26 s for the B picks, and 0.33 s for the C picks). The individual measurements are still quite scattered, so, in order to identify lateral variations in attenuation, we apply a stacking procedure as described in the next section.

Stacking to Reveal Lateral Variability of t^*

The experiments with synthetic data sets indicate that the measurement techniques are capable of giving relatively unbiased observations, yet application to real data sets yields considerable scatter in t^* measurements. A few extremely clean waveforms give t^* observations which are insensitive to the measurement technique and to the details of the chosen fitting window. Such measurements are rare, and a stacking method must be used on the bulk of the data to obtain more stable results. Generally, single-record estimates of t^* are relatively poorly constrained (although the use of multitapers gives more stable results than single-taper estimates).

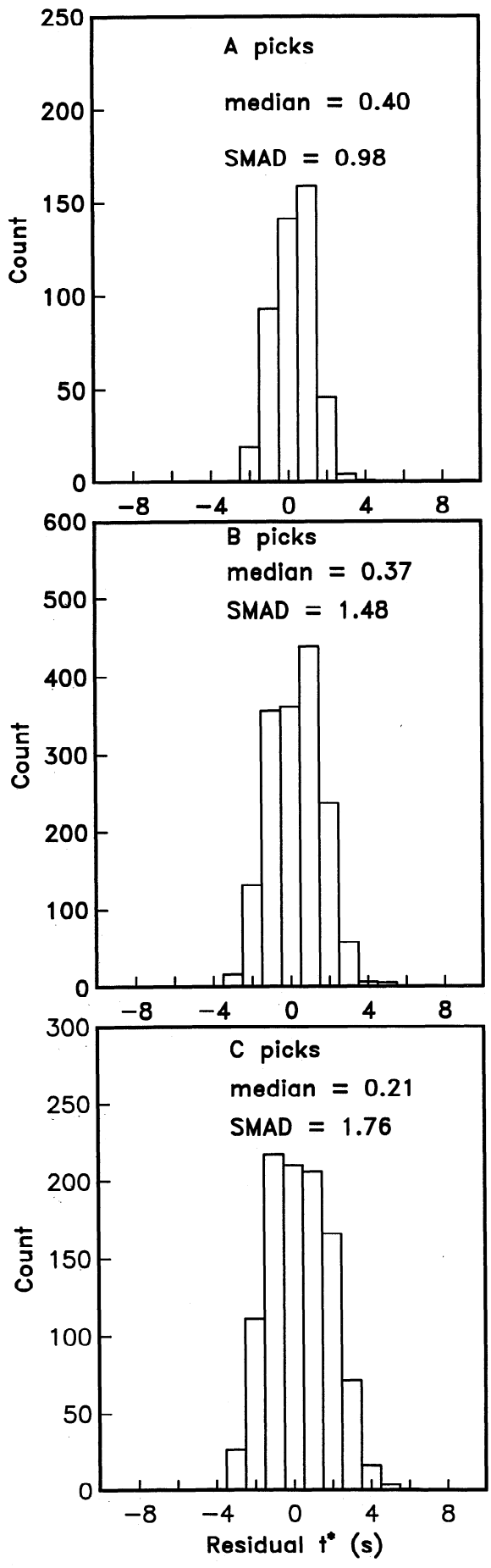

Inspection of the slopes of the amplitude variation as a function of frequency indicates that single-record estimates rarely show a simple linear behavior but stacking appears to improve the situation [*Jordan and Sipkin*, 1977; *Flanagan and Wiens*, 1994]. It is straightforward to combine several recordings with similar ray geometry or common SS bounce points to solve for a single value of t^*. In this section, we adopt a weighted stacking procedure where each measurement is weighted by the average error estimate of its assigned grade. We use two different stacking procedures: (1) we find the best fitting slope to the stacked spectral amplitudes and (2) we solve for multiple transfer functions with common t^* values.

We group the data by SS bounce point location, implicitly assuming that t^* variations are accumulated mainly in the upper mantle beneath the bounce points. For a series of 1668 locations at 5° spacing, we find those seismograms with bounce point positions within a circular cap of 5° radius and apply the multiple-record stacking techniques to compute a robust estimate of the cap-averaged t^*. There is some overlap in data between adjacent caps. We use only those caps that have at least five measurements; our final analysis uses 537 caps with some having nearly 150 individual bounce points. As the horizontal wavelengths of the SS phase are of the order of 200 to 250 km (and the effective Fresnel zone is much larger), our measurements are quite insensitive to rapid variations of attenuation and more importantly to the scattering from small-scale structures beneath the SS bounce points.

Figure 6 shows a histogram of the cap-averaged residual t^* values, which vary between -1.5 and 2.0 s (relative to the reference spherical model, PREM). The SMAD of the distribution is 0.55 s which is about a factor of 2 larger than the typical precision of a cap value. This implies that we can resolve signal from 3-D structure. It is interesting to note that a t^* variation of 0.55 s results in a travel time variation due to physical dispersion of about 0.5 s [*Minster*, 1980] which is about a tenth of a typical $SS - S$ travel time residual [*Woodward and Masters*, 1991].

To check the stability of our cap-averaged values, we computed t^* averages within 2° spherical caps. Though the number of caps (with at least five picks) is much smaller, we observe that the patterns and average values are essentially the same as before. As a further test to check for the effects of interference from nearby phases, we divide our residuals into two distance ranges (45°–85° and 85°–102°) and constructed cap-averaged t^* maps for both sets. Despite some differences in the upper mantle coverage of the caps, the patterns in the

Figure 5. Histogram of individual A, B, and C quality $SS - S$ residual t^* measurements. The average values of these measurements are quite close, though the spread of the distributions increases for lower quality measurements.

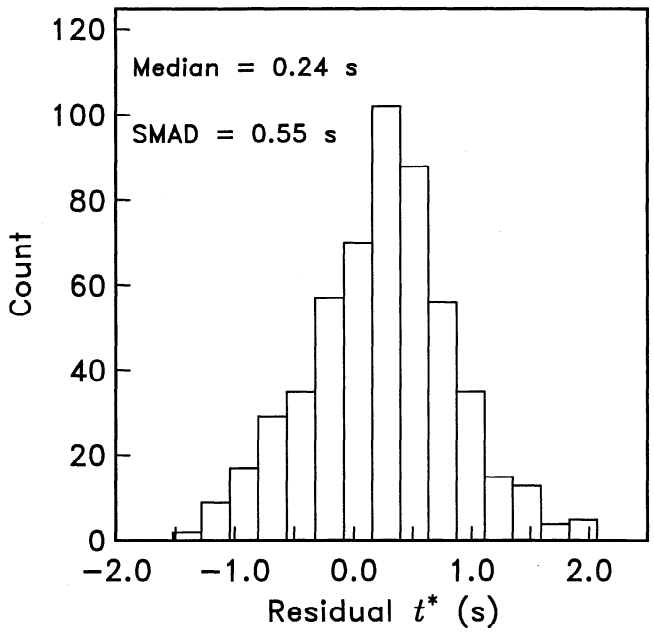

Figure 6. Distribution of cap-averaged residual t^* values computed from stacked amplitude spectra. On average, we observe slightly higher attenuation than predicted by PREM.

maps correlate well. The average value is lower by about 0.2 s for the data set with larger epicentral distance, possibly due to contamination from ScS or to the different geographic coverage. The distributions of cap-averaged t^* values are similar; thus the possibility of ScS distorting the back end of the S waveform does not seem to introduce significant scatter into our measurements.

To emphasize lateral variations in t^*, we subtract the effect of a radially symmetric reference attenuation model (PREM) from our measurements. Figure 7 shows a map of the cap-averaged t^* values computed from stacking using amplitudes alone. The mean value of the caps (0.245 s) has been removed before plotting. The stacks using both amplitude and phase data give very similar results to Figure 7, but for reasons we do not fully understand, the caps tend to show less geographical consistency. From this, we infer that phase is more susceptible to bias from interfering arrivals and that using amplitude information alone gives the most robust results.

We observe coherent large-scale patterns in the cap averages which show some correlation with tectonic features. For example, there is lower attenuation under the Eurasian and South American shield, Japan-Kurile trench, Antarctica, western Australia, the Himalayas, Indonesia, Arabian Peninsula, subduction zones in the eastern Pacific, and slow spreading centers (Mid-Atlantic and Reykjanes ridges). Prominent highs are observed under China, eastern Australia, Mexico and tectonic northern South America, the central Pacific, triple junctions (e.g., Galapagos, Azores, and Indian Ocean), and some fast spreading centers (e.g., Pacific-Antarctic Ridge). We also observe a large-scale feature with higher t^* values (i.e., high attenuation) southeast of Hawaii. This region coincides with the South Pacific

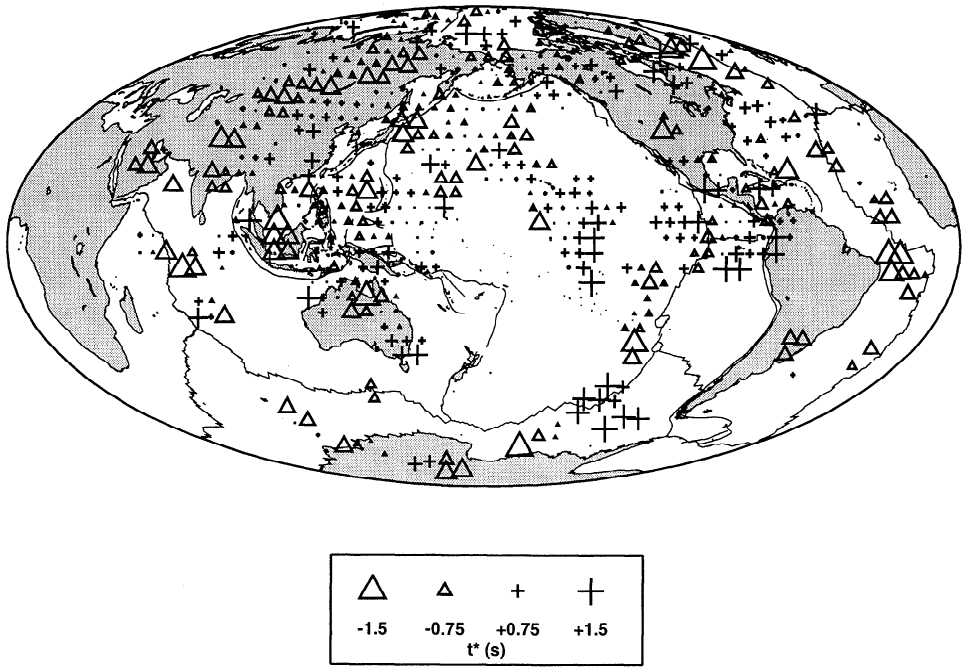

Figure 7. Map of cap-averaged residual t^* values (with respect to the reference radial Q_β model of PREM) computed from stacked amplitude spectra averaged in spherical caps of 5° radius. The mean of the cap-averaged t^* values (0.24 s) is subtracted from the values before plotting. Each of the caps have at least five measurements.

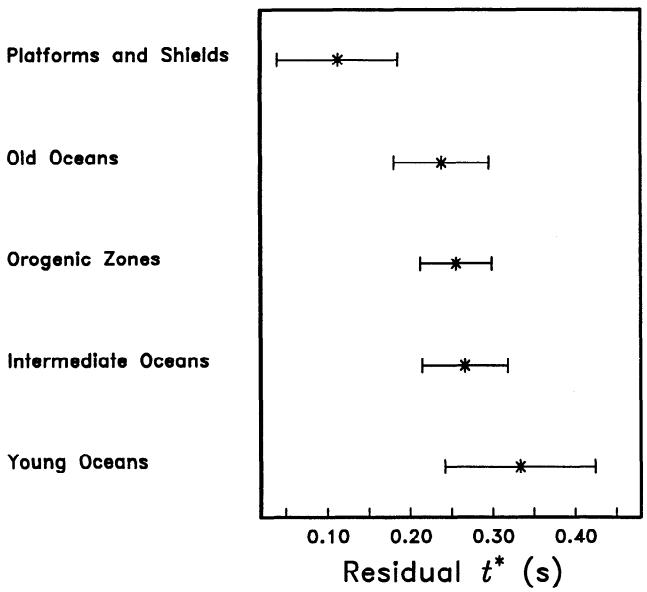

Figure 8. The average t^* residual when grouped by the tectonic regions of GTR1 along with their standard errors. Owing to the smaller number of caps, the Precambrian shields and the Phanerozoic platforms are combined into one region. We observe a distinct difference in attenuation between young oceans and platforms and shields.

"superswell" [*McNutt and Fischer*, 1987], and a number of recent studies have documented this as a region of low Q_β [*Roult et al.*, 1990; *Suda et al.*, 1991; *Bussy et al.*, 1993; *Durek et al.*, 1993; *Romanowicz*, 1994b, 1995]. The higher attenuation is most likely explained as a direct consequence of elevated temperatures [*Romanowicz*, 1994b] as expected for a region with a large number of "hot spots."

To quantify the correlation with tectonics, we use the regionalization GTR1 of *Jordan* [1981]. This regionalization consists of three oceanic regions (young, intermediate, and old oceans) and three continental regions (Precambrian shields and platforms, Phanerozoic platforms, and Phanerozoic orogenic zones and magmatic belts). We have separately grouped the cap-averaged t^* measurements in these regions. Since we have only a few caps in the Precambrian shields, these caps are combined with those in the Phanerozoic platforms. The number of caps in a region varies from 63 for young oceans to 168 for orogenic zones. Figure 8 shows the average t^* residuals for the different regions along with their standard errors. The main feature of Figure 8 is the large difference in attenuation between young oceans and platforms and shields. A similar result, with larger difference, was obtained by *Revenaugh and Jordan* [1991] from *ScS* reverberations, and our results are also consistent with earlier work by *Nakanishi* [1989b] and *Dziewonski and Steim* [1982] using surface waves. The other regions are relatively indistinct, and the distributions of t^* values strongly overlap. In particular, our data do not support large differences in integrated upper mantle attenuation between old oceans, orogenic zones, and intermediate oceans.

Upper Mantle Q Structure: Comparison With Previous Work

Comparison With Q_{ScS} Studies

For ease of comparison, we convert our t^* values to a map of $q_{ScS} = 1000/Q_{ScS}$. To do this, we assume that all the variability in attenuation occurs above a depth of 660 km and that the lower mantle has a constant Q value (adjusted to give the observed mean Q_{ScS}). We then find the geographic variation of $q = 1000/Q_\beta$ in the top 660 km which matches the observed t^* cap values and compute a q_{ScS} for each cap. The final q_{ScS} values have a mean of 4.8 and range from 3.7 to 6 (Figure 9a). As expected, the pattern of q_{ScS} variation is nearly proportional to the t^* variations (shown in Figure 7).

Figure 9b shows the results of several studies which have used the attenuation of ScS multiples to estimate q_{ScS}. A total of 54 measurements have been extracted from the literature [*Nakanishi*, 1979a; *Sipkin and Jordan*, 1980; *Lay and Wallace*, 1983, 1988; *Chan and Der*, 1988; *Revenaugh and Jordan*, 1989, 1991; *Sipkin and Revenaugh*, 1994]. Since these studies effectively sample a corridor between source and receiver, we have placed each q_{ScS} value at the center of the corridor sampled by the particular experimental geometry. These values are much more variable than our inferred q_{ScS} map and range from 2.8 to 10.8 with a mean of 5.3. These extreme variations are difficult to explain physically, and there are often discrepancies between the different studies. The large differences between Figures 9a and 9b are difficult to explain, though part of the problem may be the wide range of experimental techniques that have been employed in the ScS studies.

Comparisons With Global Surface Wave Attenuation Studies

Recently, *Romanowicz* [1995] has published a 3–D model of shear attenuation in the upper mantle (named QR19), based on an inversion of surface wave amplitudes. QR19 is a global model which contains smooth, large-scale (up to $\approx$ degree 6) variations of Q_β. To compare our results to the predictions of this model, we compute the $SS - S$ residual t^* predicted by QR19 for each of our seismograms and plot the cap-averaged values (Figure 10). The plotted values are reduced by the mean cap-averaged t^* which is slightly higher (0.16 s) than our observations.

A comparison of Figures 7 and 10 shows that, as might be expected, the Q model predicts smaller and smoother variations in t^* than are observed though there are many similarities in the large-scale patterns of lateral variations. For example, both maps show lower attenuation under the Eurasian shield, the Himalayas,

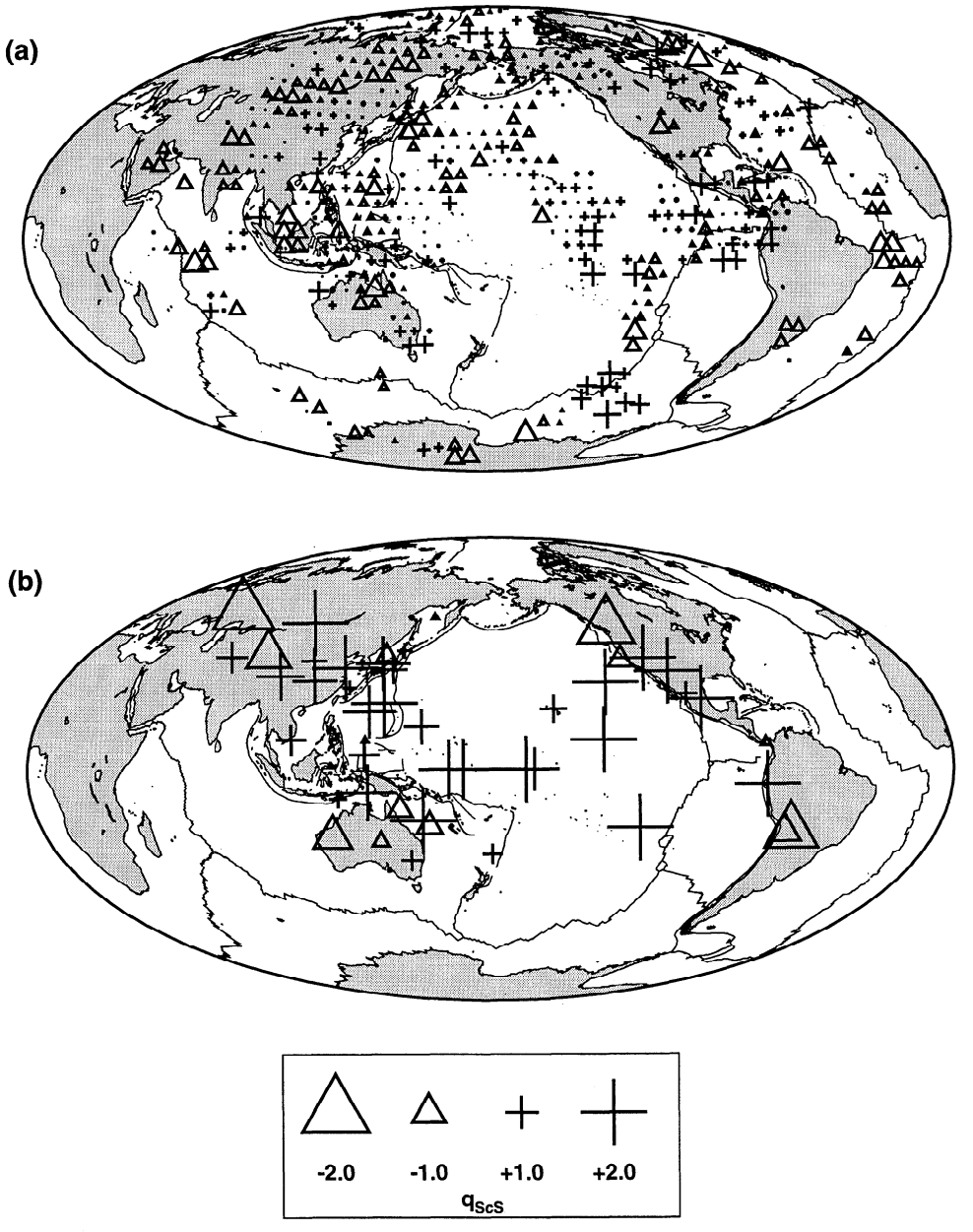

Figure 9. Comparison of q_{ScS} (= $1000/Q_{ScS}$) inferred from our measurements with values taken from the literature. (a) Map of q_{ScS} computed from the measured t^* values (see text). The values are reduced by their mean (4.8 s). (b) Map of published q_{ScS} values plotted at the middle of the source-receiver corridor sampled by each experiment. These values have also been reduced by 4.8 s.

and western Australia and highs under the mid-Pacific (south of Hawaii), China, and eastern Australia. The primary differences are under the subduction zones in the western Pacific and the young oceans in the mid and South Pacific. To quantify the correlation between the maps, we use the spherical spline analysis of *Parker* [1994] to compute the smoothest residual t^* patterns that fit the data and the predictions of QR19. The equivalent spherical harmonic expansions of the splined fields are easy to compute and allow the computation of the degree-by-degree correlation (Figure 11a). From this, we conclude that the maps in Figures 7 and 10 are slightly correlated at degrees 1 and 4, while the correlations decrease for degrees 2 and 5 and are poor at other degrees. It remains to be seen if there is a q model which is capable of fitting both the surface wave data and the $SS - S$ data.

We have also compared our maps with the results of *Durek et al.* [1993]. They used Rayleigh wave amplitude measurements to present even order (i.e., degrees 0, 2, 4, 6) maps of q variations in the upper mantle at periods of 160 s, 200 s, and 240 s. The correlation between the maps, shown in Figure 11b, is good at degree 2 for long periods but is insignificant at degrees 4 and 6.

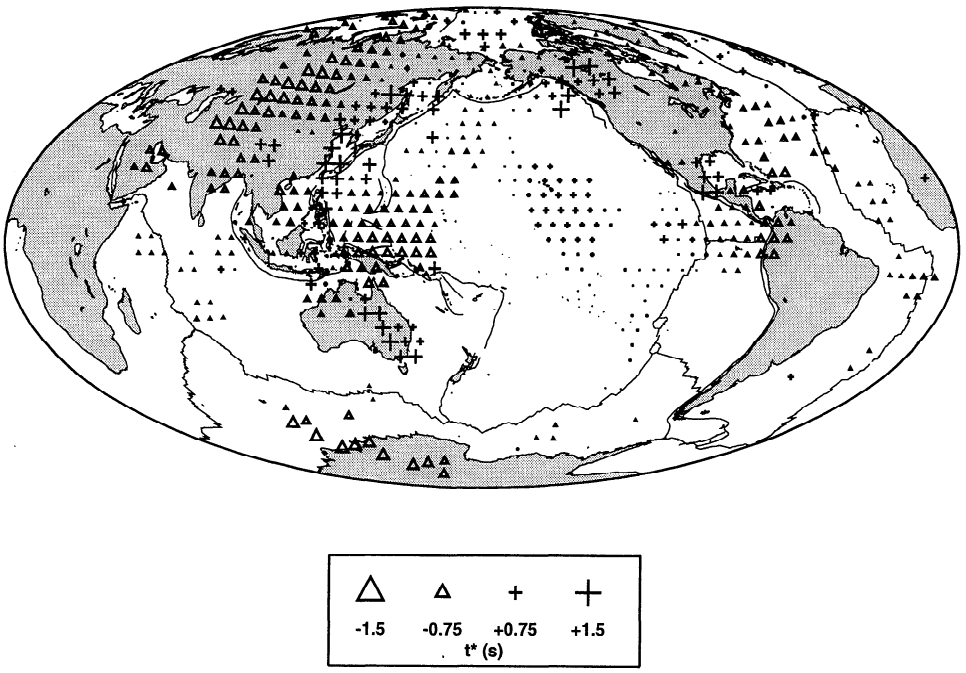

Figure 10. Average t^* values predicted by model QR19 [*Romanowicz*, 1995] plotted at 5° caps. The average value (0.4 s) has been subtracted before plotting. This map compares favorably with Figure 7, though the latter shows some shorter-wavelength features.

Comparisons With Global Velocity Studies

A positive correlation between higher attenuation and slower velocities is expected if both are primarily due to lateral variations in temperature. We explore this by comparing our SS versus S map of t^* variations (Figure 7) with a map of $SS - S$ travel time residuals (Figure 12). Note that Figure 12 has been corrected for the effects of lower mantle structure using the model $S16B30$ of *Masters et al.* [1996]. Both the t^* and travel time residuals are likely dominated by variations in the upper mantle beneath the SS bounce points, though the largest variations in attenuation are likely to be deeper than the largest variations in velocity. Although the coverage in the maps differs, the trends shown by the large-scale features correlate weakly between the maps. Negative travel time residuals are observed for regions with negative t^* residuals under Eurasia, the Himalayas,

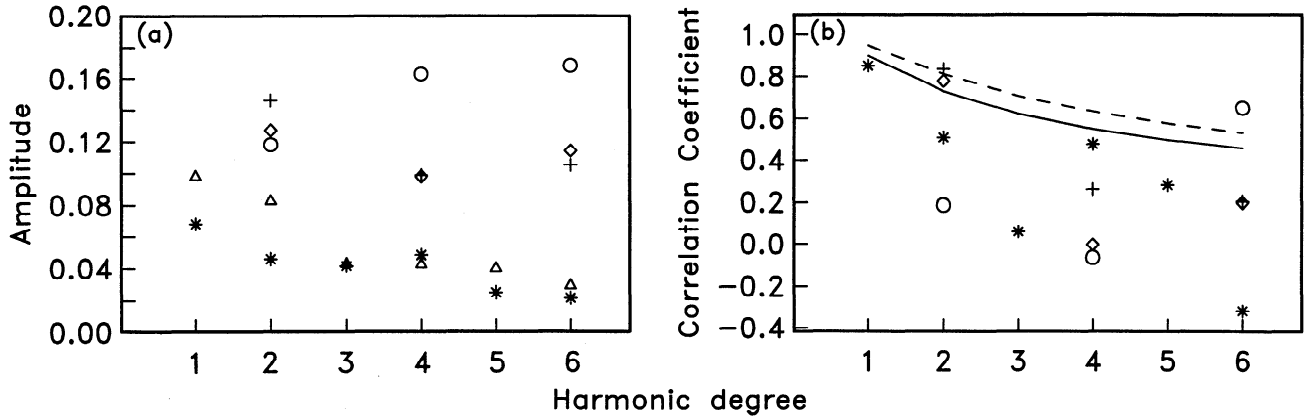

Figure 11. Correlation and amplitude of the t^* map (Figure 7) compared with maps of upper mantle shear wave attenuation as a function of harmonic degree. (a) Amplitude spectrum of the map of measured t^* values (triangles), the map of predicted t^* using model QR19 of *Romanowicz* [1995] (asterisks), and maps of q variations from [*Durek et al.*, 1993] at different periods : 160 s (circles), 200 s (diamonds), and 250 s (crosses). (b) Correlation coefficient of the t^* map with the other maps. The symbol convention is as in Figure 11a. The significance levels as a function of harmonic degree are shown by the solid (90%) and dashed (95%) lines. The higher correlation between the maps at degrees 1 and 2 is significant since the t^* map is dominated by signal at these two degrees.

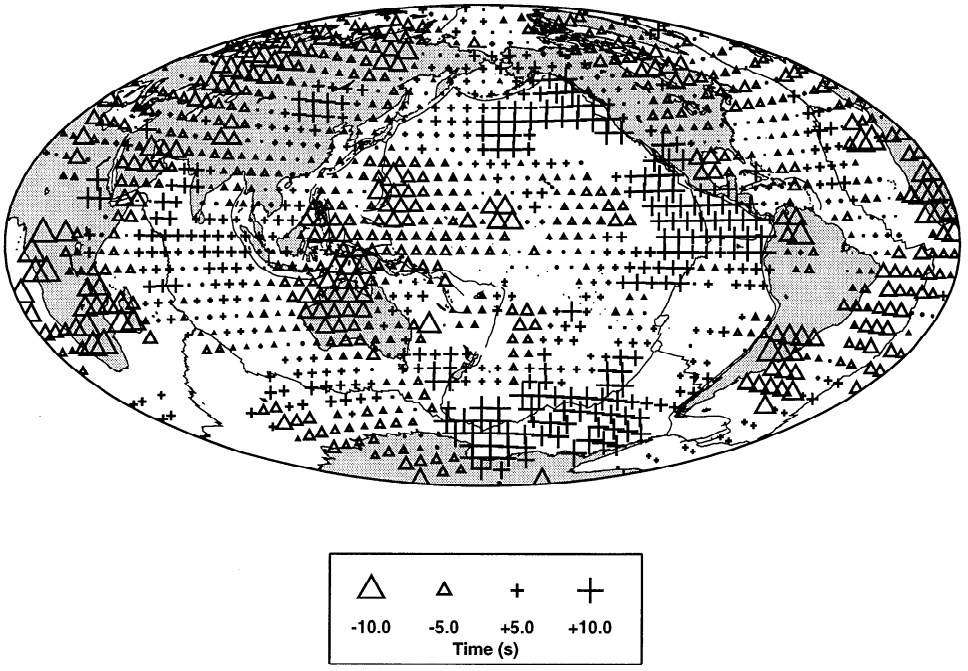

Figure 12. Lower mantle corrected $SS - S$ residual travel times. The data set is an much expanded version of the one given by *Woodward and Masters* [1991], and the data have been corrected using model $S16B30$ of *Masters et al.* [1996]. The average travel time residual has been subtracted before plotting, and the data have been averaged by bouncepoint location into 5° radius caps. (Only caps with at least three measurements are plotted.)

the northern Arabian peninsula, South America, the Mid-Atlantic Ridge, and western Australia. Positive residuals in the maps correlate under the mid-Pacific, China, eastern Australia, the Pacific-Antarctic ridge, and the Bering Sea.

We also compare our map of computed q values with maps of lateral variations of shear wave velocities of the model $S16B30$ [*Masters et al.*, 1996] at different upper mantle depths. The correlation coefficients between the maps as a function of harmonic degree are shown in Figure 13. The correlations are significant only at degrees 1 and 2. It is interesting to note that the highest correlations for degree 2 are seen in the depth range of 350–600 km. This implies that at least part of the long-wavelength contribution to attenuation has a deep origin. In contrast, *Durek et al.* [1993] found that the source region of shear attenuation lies in the shallower asthenospheric region between 80 and 220 km.

Upper Mantle Shear Wave Attenuation Model

We conclude our analysis of the $SS - S$ differential t^* values by performing a preliminary inversion for q_β $(= 1000/Q_\beta)$ in the upper mantle. Since we have little depth resolution, we have used a layer parameterization similar to the reference model PREM, with the upper mantle being divided into three layers with depths 20-220 km, 220-400 km, and 400-670 km. We first solve for the best 1-D model that fits our data, and to do this, we look for small perturbations to existing Q models which were designed to fit free oscillation and/or surface wave data. Three initial models are considered: QM1 [*Widmer et al.*, 1991], QL6 [*Durek and Ekstrom*, 1996], and the radially averaged values of the three-dimensional upper mantle model, QR19 [*Romanowicz*, 1995]. These models (averaged into our three layers) are plotted in Figure 14 along with the final values obtained after inversion. We have shown the radially symmetric PREM model in Figure 14b for reference. Clearly, all the final models are very similar and look most like models de-

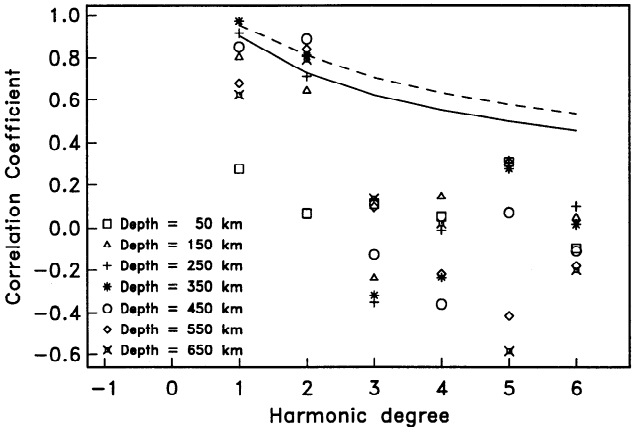

Figure 13. Correlation of the t^* map of Figure 7 with different depth slices of the model of lateral shear velocity variations of *Masters et al.* [1996]. The maps are significantly correlated at degrees 1 and 2 with the best correlation at depths of 250–550 km.

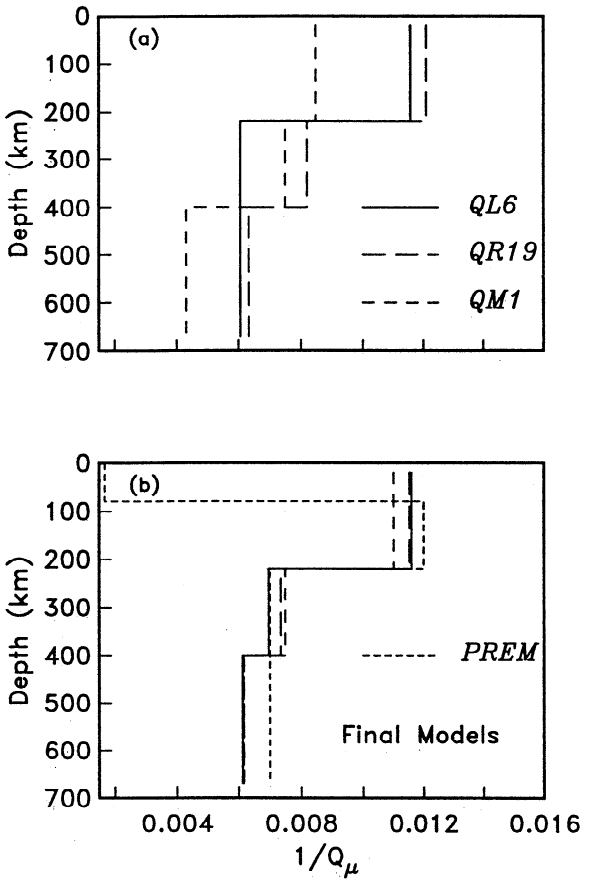

Figure 14. Results of a 1-D inversion using the measured t^* values. (a) The three starting models: QM1, QL6, and QR19. (b) The three final models along with the radial reference model, PREM. These models are all quite similar and look more like models derived from surface wave studies (QL6 and QR19) than the models derived from free oscillations.

rived from surface waves (QL6) rather than the models derived from free oscillations (QM1). Smoother models or models with different layer spacing can undoubtedly be obtained than can fit the data equally well, but the t^* data set does not have the vertical resolution to choose between them. We use the mean of the three final models as the base model for an inversion for three-dimensional structure. This model fits our body wave data set better than PREM, and we obtain an average Q_β value of 112 in the upper 400 km of the mantle (compared to the PREM value of 128).

We parameterize the lateral variation in attenuation, q_β , in the kth layer as a sum of spherical harmonics (truncated at degree 8)

$$q_k(\theta,\phi) = \sum_{l,m} q_l^m(k) Y_l^m(\theta,\phi) \tag{7}$$

Thus the measured residual t^* for the jth seismogram can be written in terms of perturbations from a reference radially symmetric Q_β model as

$$\begin{aligned} \delta t_j^* &= t_j^* - t_{\text{ref}}^* \\ &= \sum_{l=0}^{8} \sum_{m=-l}^{+l} \sum_{k=1}^{3} \delta q_l^m(k) \int_{r_k}^{r_{k+1}} \frac{1}{v(r)} Y_l^m(\theta,\phi) d\tau \end{aligned} \tag{8}$$

where t_{ref}^* is the t^* value predicted by the reference model, r_k is the radius of the kth knot, $v(r)$ is the shear wave velocity at radius r, and the integration is computed along the ray path. We include the $l = 0$ term in the expansion to allow small variations away from our average one-dimensional model if these are required by the inversion (note that the one-dimensional inversion took no account of the geographic variation in the t^* data).

The forward problem for the t^* perturbations due to aspherical structure is computed using the linearized theory given by *Dziewonski* [1984] for the travel time problem allowing equation (8) to be written in matrix form as

$$\delta \mathbf{t}^* = \mathbf{B} \cdot \delta \mathbf{q} \tag{9}$$

where $\delta \mathbf{q}$ is the vector of spherical harmonic coefficients describing the three-dimensional q structure. The inverse solution to equation (9) is obtained following the method of *Woodward and Masters* [1992] which is based on the philosophy of "Occam's inversion" given by *Constable et al.* [1987]. In this method, we desire a solution which minimizes the misfit to within a prescribed tolerance, (i.e., using χ^2 as a measure of expected misfit), while simultaneously minimizing a measure of roughness of the model. Since we normalize the residuals by the errors of the individual measurements, after inversion, χ^2 should be approximately equal to the number of data used. Following *Woodward and Masters* [1992], we look for models which minimize the squared surface Laplacian integrated over the sphere and which minimize the first radial difference of structure between adjacent layers.

After removal of a few outliers, the final data set used for inversion consisted of 2724 residuals. Since we are using individual seismograms in our inversion, we scale the errors used in the stacking experiment by a factor of $\sqrt{N}$, where N is the average number of measurements in a cap. Thus the errors for the A, B, and C picks are 0.73 s, 1.05 s, and 1.34 s respectively. We seek solutions which have a χ^2 value of about 2724 and satisfy the physical constraint of nonnegative attenuation value at every point in the model. All such solutions look like the model shown in Figure 15 which has a χ^2 value of 2827. Note that the top two layers of this model are very similar to one another, while the third is quite different. Resolution experiments indicate that the third layer of the model is best resolved, while the top two layers cannot be distinguished from one another with the current data set. While this experiment shows that it is possible to find smooth models of q structure in the

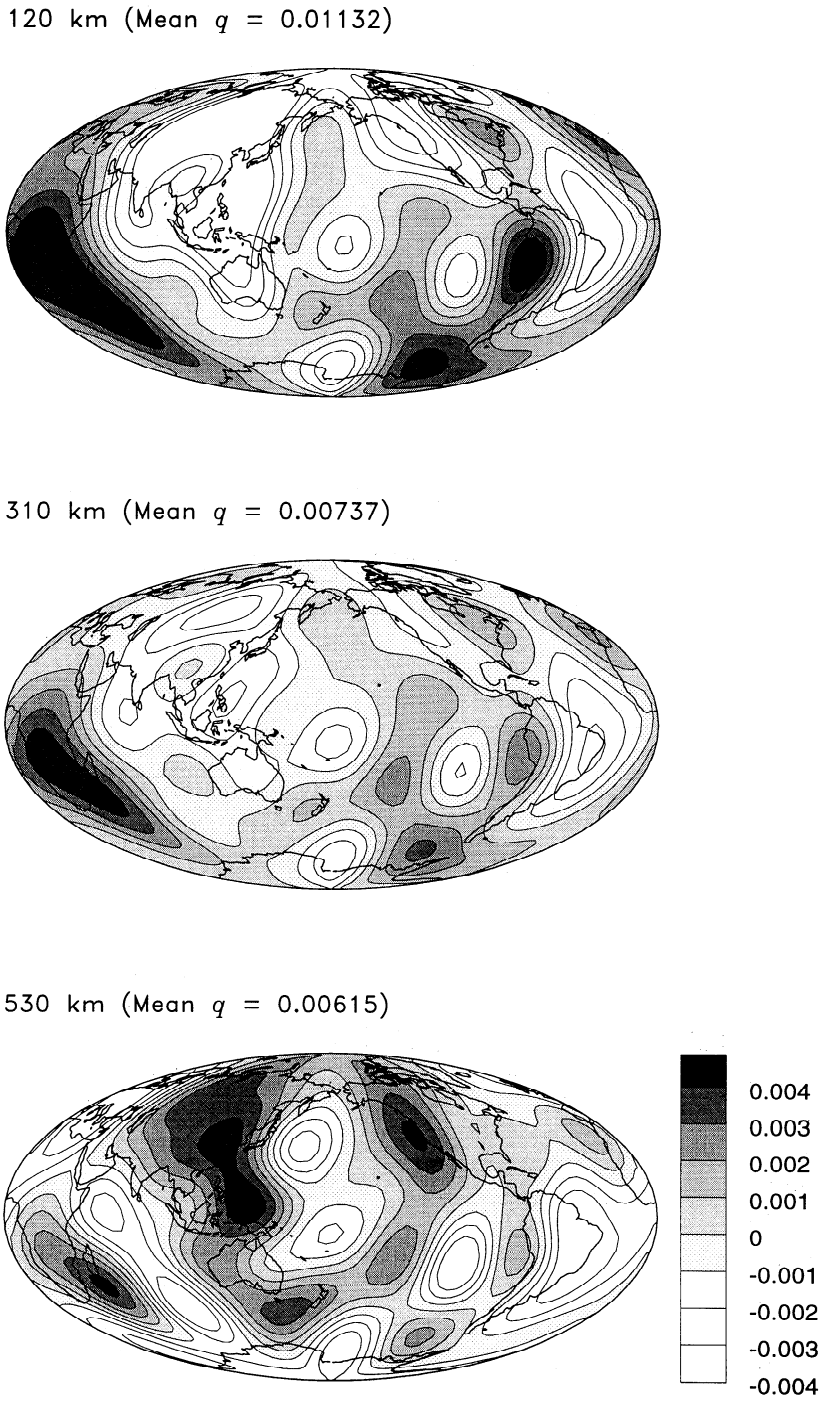

Figure 15. Three-layered upper mantle q_β models presented as perturbations from a reference radially symmetric q_β model (which is the average of the models shown in Figure 14b). The numbers on the maps show the depth at the middle of the layer and the layer-averaged q_β value.

upper mantle that fit the data, resolution of structure will require the addition of other types of data in the inversion (e.g., surface wave data).

Conclusions

The following are the main results of the study:

1. We have developed a frequency domain measurement technique (in the 0.02 to 0.1 Hz range) capable of giving relatively stable estimates of t^* from long-period waveforms. The effect of interference from nearby waveforms is reduced, and the scatter in the measurements is much smaller than for time domain measurements.

2. We adopt a stacking technique to compute lateral variations of t^*. The cap-averaged residual t^* has an average value of 0.24 s with individual cap values ranging between -1.4 s and 1.8 s. These lateral variations in

attenuation, through physical dispersion, could account for about 10% of the signal seen in the travel times of shear waves which sample the upper mantle.

3. We observe that the t^* residuals correlate with tectonic regionalization. Significantly higher attenuation is observed under young oceans compared to continental platforms and shields. Also, there is a systematic (but weak) dependence of residual size on age of the oceanic lithosphere. On the other hand, correlation of the t^* map with 3-D velocity models gives the best correlation at depths lower than 300 km (though correlation is significant only at degrees 1 and 2).

4. A map of q_{ScS} inferred from our measurements is poorly correlated with direct measurements of the attenuation of ScS multiples reported in the literature and shows much less variability than the published values.

5. One-dimensional Q models derived from our data agree well with models deduced from surface wave observations and less well with Q models deduced from free oscillation measurements. Our data can be modeled by large-scale lateral variations in shear attenuation in the upper mantle but cannot by themselves resolve such structure in depth. The addition of surface wave attenuation data should do much to improve this situation.

Acknowledgments. This research has been supported by grant EAR94-05948 from the National Science Foundation. We thank Barbara Romanowicz for sending us the attenuation model QR19. This manuscript has benefitted from the constructive reviews of the two anonymous referees and the Associate Editor, Steven Roecker. We thank Harold Bolton and Stuart Johnson for help with inverting the t^* data and Megan Flanagan for reviewing an earlier version of this manuscript.

References

Anderson, D.L., and C.B. Archambeau, The anelasticity of the Earth, *J. Geophys. Res., 69*, 2071–2084, 1964.

Anderson, D.L., and J.W. Given, Absorption band Q model for the Earth, *J. Geophys. Res., 87*, 3893–3904, 1982.

Anderson, D.L., and R.S. Hart, Q of the Earth, *J. Geophys. Res., 83*, 5869–5882, 1978.

Anderson, D.L., and J.B. Minster, Seismic velocity, attenuation and rheology in the upper mantle, in *Source Mechanism and Earthquake Prediction*, edited by C.J. Allègre, pp. 13–22, Cent. Nat. Rech. Sci., Paris, France, 1980.

Anderson, D.L., A. Ben-Menahem, and C.B. Archambeau, Attenuation of seismic energy in the upper mantle, *J. Geophys. Res., 70*, 1441–1448, 1965.

Anderson, D.L., H. Kanamori, R.S. Hart, and H.-P. Liu, The Earth as a seismic absorption band, *Science, 196*, 1104–1106, 1977.

Bhattacharyya, J., P.M. Shearer, and G. Masters, Inner core attenuation from short period $PKP(BC)$ versus $PKP(DF)$ waveforms, *Geophys. J. Int., 114*, 1–11, 1993a.

Bhattacharyya, J., G. Masters, and P.M. Shearer, Upper mantle attenuation from long-period $SS - S$ differential waveforms (abstract), *Eos Trans. AGU, 74*(43), Fall Meet. Suppl., 439, 1993b.

Bussy, M., J.P. Montagner, and B. Romanowicz, Tomographic study of upper mantle attenuation in the Pacific Ocean, *Geophys. Res. Lett., 20*, 663–666, 1993.

Canas, J.A., and B.J. Mitchell, Lateral variation of surface-wave anelastic attenuation across the Pacific, *Bull. Seismol. Soc. Am., 68*, 1637–1650, 1978.

Canas, J.A., and B.J. Mitchell, Rayleigh wave attenuation and its variation across the Atlantic Ocean, *Geophys. J. R. Astron. Soc., 67*, 159–176, 1981.

Chan, W. W., and Z.A. Der, Attenuation of multiple ScS in various parts of the world, *Geophys. J. Int., 92*, 303–314, 1988.

Choy, G.L., and P.G. Richards, Pulse distortion and Hilbert transformation in multiply reflected and refracted body waves, *Bull. Seismol. Soc. Am., 65*, 55–70, 1975.

Constable, S.C., R.L. Parker, and C.G. Constable, Occam's inversion; A practical algorithm for generating smooth models from electromagnetic sounding data, *Geophysics, 52*, 289–300, 1987.

Ding, X.-Y., and S.P. Grand, Upper mantle Q structure under the East Pacific Rise, *J. Geophys. Res., 98*, 1973–1985, 1993.

Doornbos, D.J., Observable effects of the seismic absorption band in the Earth, *Geophys. J. R. Astron. Soc., 75*, 693–711, 1983.

Durek, J.J., and G. Ekstrom, A radial model of anelasticity consistent with long-period surface-wave attenuation, *Bull. Seismol. Soc. Am., 86*, 144–158, 1996.

Durek, J.J., M.H. Ritzwoller, and J.H. Woodhouse, Constraining upper mantle anelasticity using surface wave amplitudes, *Geophys. J. Int., 114*, 249–272, 1993.

Dziewonski, A.M., Mapping the lower mantle: determination of lateral heterogeneity in P velocity upto degree and order 6, *J. Geophys. Res., 89*, 5929–5952, 1984.

Dziewonski, A.M., and D.L. Anderson, Preliminary reference Earth model, *Phys. Earth Planet. Inter., 25*, 297–356, 1981.

Dziewonski, A.M., and J. Steim, Dispersion and attenuation of mantle waves through waveform inversion, *Geophys. J. R. Astron. Soc., 70*, 503–527, 1982.

Dziewonski, A.M., A.L. Hales, and E.R. Lapwood, Parametrically simple Earth models consistent with geophysical data, *Phys. Earth Planet. Inter., 10*, 12–48, 1975.

Efron, B., *The Jackknife, the Bootstrap and Other Resampling plans*, Ser. Appl. Math., vol. 38, Soc. for Ind. and Appl. Math., Philadelphia, Pa., 1982.

Flanagan, M.P., and D.A. Wiens, Attenuation structure beneath the Lau back-arc spreading center from teleseismic S phases, *Geophys. Res. Lett., 17*, 2117–2120, 1990.

Flanagan, M.P., and D.A. Wiens, Radial upper mantle structure of inactive back-arc basins from differential shear wave measurements, *J. Geophys. Res., 99*, 15,469–15,485, 1994.

Futterman W.I., Dispersive body waves, *J. Geophys. Res., 67*, 5279–5291, 1962.

Jeffreys, H., Damping of S waves, *Nature, 208*, 675, 1965.

Jordan, T.H., Global tectonic regionalization for seismological data analysis, *Bull. Seismol. Soc. Am., 71*, 1131–1141, 1981.

Jordan, T.H., and S.A. Sipkin, Estimation of the attenuation operator for multiple ScS waves, *Geophys. Res. Lett., 4*, 167–170, 1977.

Kanamori, H., and D.L. Anderson, Importance of physical dispersion in surface-wave and free oscillation problems, *Rev. Geophys., 15*, 105–112, 1977.

Karato, S., Importance of anelasticity in the interpretation of seismic tomography, *Geophys. Res. Lett., 20*, 1623–1626, 1993.

Karato, S., and H.A. Spetzler, Defect microdynamics in minerals and solid-state mechanisms of seismic wave attenuation and velocity dispersion in the mantle, *Rev. Geophys., 28*, 399–421, 1990.

Kleiner, B., and T.E. Graedel, Exploratory data analysis

in the geophysical sciences, *Rev. Geophys., 18*, 699–717, 1980.

Kovach, R.L., and D.L. Anderson, Attenuation of shear waves in the upper and lower mantle, *Bull. Seismol. Soc. Am., 54*, 1855–1865, 1964.

Lamb, G.L., The attenuation of waves in a dispersive medium, *J. Geophys. Res., 67*, 5273–5278, 1962.

Lawson, C.L., and R.J. Hanson, *Solving Least Squares Problems*, Prentice-Hall, Englewood Cliffs, N.J., 1974.

Lay, T., and T.C. Wallace, Multiple *ScS* travel times and attenuation beneath Mexico and Central America, *Geophys. Res. Lett., 10*, 301–304, 1983.

Lay, T., and T.C. Wallace, Multiple *ScS* attenuation and travel times beneath western north America, *Bull. Seismol. Soc. Am., 78*, 2041–2061, 1988.

Liu, H., D.L. Anderson, and H. Kanamori, Velocity dispersion due to anelasticity: Implications for seismology and mantle composition, *Geophys. J. R. Astron. Soc., 47*, 41–58, 1976.

Lomnitz,C., Linear dissipation in solids, *J. Appl. Phys., 28*, 201–205, 1957.

Lundquist, G.M., and V.C. Cormier, Constraints on the absorption band model of *Q*, *J. Geophys. Res., 85*, 5244–5256, 1980.

Masters, G., S. Johnson, G. Laske, and H. Bolton, A shear-velocity model of the mantle, Philos. Trans. R. Soc. London, in press, 1996.

McNutt, M.K., and K.M. Fischer, The South Pacific superswell, in *Seamounts, Islands, and Atolls, Geophys. Monogr. Ser.*, vol. 43, edited by B.Keating, P. Fryer, R. Batiza, and G.W. Boehlert, pp. 25–34, AGU, Washington, D.C., 1987.

Minster, J.B., Anelasticity and attenuation, in *Physics of the Earth's Interior*, edited by A.M. Dziewonski and E. Boschi, pp. 152–212, North-Holland Publ. Co., Amsterdam, 1980.

Minster, J.B., and D.L. Anderson, A model of dislocation-controlled rheology for the mantle, *Philos. Trans. R. Soc. London, 299*, 319–356, 1981.

Mitchell, B.J., Regional Rayleigh wave attenuation in North America, *J. Geophys. Res., 80*, 4904–4916, 1975.

Mitchell, B.J., N.K. Yacoub, and A.M. Correig, A summary of seismic surface wave attenuation and its regional variation across continents and oceans, in *The Earth's Crust: Its Nature and Physical Properties, Geophys. Monogr. Ser.*, vol. 20, edited by J.G. Heacock, pp. 405–423, AGU, Washington, D.C., 1977.

Nakanishi, I., Attenuation of multiple *ScS* waves beneath the Japanese arc, *Phys. Earth Planet. Inter.*, 19, 337–347, 1979a.

Nakanishi, I., Phase velocity and *Q* of mantle Rayleigh waves, *Geophys. J. R. Astron. Soc., 58*, 35–59, 1979b.

Parker, R.L., *Geophysical Inverse Theory*, Princeton Univ. Press, Princeton, N.J., 1994.

Randall, M.J., Attenuative dispersion and frequency shifts of the Earth's free oscillations, *Phys. Earth Planet. Inter., 12*, P1–P4, 1976.

Revenaugh, J.S., and T.H. Jordan, A study of mantle layering beneath the western Pacific, *J. Geophys. Res., 94*, 5787–5813, 1989.

Revenaugh, J.S., and T.H. Jordan, Mantle layering from *ScS* reverberations, 1, Waveform inversion of zeroth-order reverberations, *J. Geophys. Res., 96*, 19,749–19,762, 1991.

Romanowicz, B., The upper mantle degree 2: Constraints and measurements from global mantle wave attenuation measurements, *J. Geophys. Res., 95*, 11,051–11,071, 1990.

Romanowicz, B., On the measurement of anelastic attenuation using amplitudes of low frequency surface waves, *Phys. Earth Planet. Inter., 84*, 179–191, 1994a.

Romanowicz, B., Anelastic tomography: A new perspective on upper-mantle thermal structure, *Earth Planet. Sci. Lett., 128*, 113–121, 1994b.

Romanowicz, B., A global tomographic model of shear attenuation in the upper mantle, *J. Geophys. Res., 100*, 12,375–12,394, 1995.

Roult, G., B. Romanowicz, and J.P. Montagner, 3-D upper mantle shear velocity and attenuation from fundamental mode free oscillation data, *Geophys. J. Int., 101*, 61–80, 1990.

Sato, H., I.S. Sacks, T. Murase, G. Muncill, and H. Fukuyama, Q_P–melting temperature relation in peridotite at high pressure and temperature: Attenuation mechanism and implications for the mechanical properties of the upper mantle, *J. Geophys. Res., 94*, 10,647–10,661, 1989.

Schlue, J.W., Differential shear-wave attenuation (delta t^*) across the East Pacific Rise, *Geophys. Res. Lett., 8*, 861–864, 1981.

Shearer, P.M., Constraints on upper mantle discontinuities from observations of long-period reflected and converted phases, *J. Geophys. Res., 96*, 18,147–18,182, 1991.

Sheehan, A.F., and S.C. Solomon, Differential shear wave attenuation and its lateral variation in the North Atlantic region, *J. Geophys. Res., 97*, 15,339–15,350, 1992.

Sipkin, S.A., Estimation of the attenuation operator for multiple-*ScS* waves using digitally recorded broadband data, *Geophys. Res. Lett., 15*, 832–835, 1988.

Sipkin, S.A., and T.H. Jordan, Frequency dependence of Q_{ScS}, *Bull. Seismol. Soc. Am., 69*, 1055-1079, 1979.

Sipkin, S.A., and T.H. Jordan, Regional variations of Q_{ScS}, *Bull. Seismol. Soc. Am., 70*, 1071–1102, 1980.

Sipkin, S.A., and J. Revenaugh, Regional variation of attenuation and travel time in China from analysis of multiple-*ScS* phases, *J. Geophys. Res., 99*, 2687–2699, 1994.

Smith, M.F., and G. Masters, Aspherical structure constraints from free oscillation frequency and attenuation measurements, *J. Geophys. Res., 94*, 1953–1976, 1989.

Suda, N., N. Shibata, and Y. Fukao, Degree-2 pattern of attenuation structure in the upper mantle from apparent complex frequency measurements of fundamental spheroidal modes, *Geophys. Res. Lett., 18*, 1119–1122, 1991.

Thomson, D.J., Spectrum estimation and harmonic analysis, IEEE Proc., *70*, 1055–1096, 1982.

Widmer, R., G. Masters, and F. Gilbert, Spherically symmetric attenuation within the Earth from normal mode data, *Geophys. J. Int., 104*, 541–553, 1991.

Woodward, R.L., and G. Masters, Global upper mantle structure from long-period differential travel times, *J. Geophys. Res., 96*, 6351–6377, 1991.

Woodward, R.L., and G. Masters, Upper mantle structure from long-period differential travel times and free oscillation data, *Geophys. J. Int., 109*, 275–293, 1992.

J. Bhattacharyya, Campus box 216, CIRES, University of Colorado, Boulder, CO 80309-0216. (e-mail: joy@mantle.colorado.edu)

G. Masters and P. Shearer, University of California, San Diego, Scripps Institution of Oceanography, IGPP A-025 La Jolla, CA 92093-0225. (e-mail: guy@mahi.ucsd.edu; shearer@mahi.ucsd.edu)

(Received October 27, 1995; revised May 17, 1996; accepted May 29, 1996.)